Eur. Phys. J. B **20**, 19–25 (2001)

**THE EUROPEAN
PHYSICAL JOURNAL B**
EDP Sciences

The chromium spin density wave: magnetic X-ray scattering studies with polarisation analysis

D. Mannix[1,2,a], P.C. de Camargo[3], C. Giles[4], A.J.A. de Oliveira[5], F. Yokaichiya[4], and C. Vettier[2]

[1] European Commission, JRC, Institute for Transuranium Elements, Postfach 2340, 76125 Karlsruhe, Germany
[2] European Synchrotron Radiation Facility, BP 220X, 38043 Grenoble, France
[3] Departamento de Física, Universidade Federal do Paraná CP 19081, 815531-990 Curitiba Parana, Brazil
[4] Instituto de Física 'Gleb Wataghin', Universidade Estadual de Campinas, CP 6165, 13083-970 Campinas, São Paulo, Brazil
[5] Departamento de Física, Universidade Federal de São Carlos, CP 676-13565-905 São Carlos, SP, Brazil

Received 22 September 2000

Abstract. We report on X-ray magnetic diffraction studies of the spin density wave antiferromagnetism formed in the conduction electron band of chromium. Non-resonant X-ray magnetic scattering was used to directly determine that chromium has zero orbital magnetisation. Furthermore, the azimuthal dependence of this scattering provides unique evidence that chromium forms a linearly polarised wave. In the vicinity of the K absorption edge, resonant X-ray magnetic scattering was observed. A consistent model of the magnetic scattering has been derived from the resonant and non-resonant magnetic amplitudes. The enhancement of the magnetic intensity arises primarily from dipole transitions from the core $1s$ level to $4p$ states. Quadrupole transitions to the magnetic $3d$ states are essentially non-existent due to their sensitivity to (and the absence of) orbital moment. This effect is predicted from atomic considerations of the $3d^5$ ($\mathbf{L} = 0$) transition metal ions.

PACS. 75.25.+z Spin arrangements in magnetically ordered materials (including neutron and spin-polarized electron studies, synchrotron-source x-ray scattering, etc.) – 75.30.Fv Spin-density waves

1 Introduction

X-ray magnetic diffraction is a powerful implement for understanding magnetically ordered structures. Non-resonant X-ray magnetic scattering (NRXMS) [1–3] inherently relates spin and orbital moments that cannot be directly accessed by its neutron scattering counterpart, while resonant X-ray magnetic scattering (RXMS) [4–6] uniquely provides element and electron shell selectivity. We have applied these elegant X-ray probes to studies of the archetypal itinerant spin density wave (SDW) antiferromagnet, chromium.

The first series of the transition metals are characterised by the gradual filling of $3d$ states. The fourth element of this period, bcc chromium, possesses an anomalous $3d^5 4s^1$ electronic structure [7], associated with the lower ground state energy of half-filled shells compared to those in which Pauli pairing occurs. Hund's rules dictate zero orbital moment ($\mathbf{L} = 0$) for this configuration. The $3d$ wave functions of the transition metals are perturbed by the crystal field potential, which disrupts spin orbit coupling and quenches the orbital moment. Spin and orbital moments are traditionally accessed by neutron magnetic form factor considerations. This dependence has been modelled for chromium using spin only radial integrals [8,9] consistent with $\mathbf{L} = 0$. A similar zero orbital moment has also been deduced from the wave-vector dependence of high energy X-rays [10]. Since, neither of these X-ray and neutron probes provide direct measurements of the spin and orbital magnetisation, the results can be ambiguous. For example, the neutron form factor of NiO [11] can only be reproduced with a quenched orbital moment ($\mathbf{L} = 0$). Nethertheless, recent NRXMS [12] measurements have demonstrated that in this material the orbital contribution to the magnetisation is as large as 17%. We have used NRXMS, using polarisation analysis at a third generation synchrotron, to confirm unambiguously that there is no orbital contribution to the chromium magnetic moment. These results are described in Section 3.

Chromium forms an itinerant incommensurate antiferromagnetic structure below its Néel temperature, $T_\mathrm{N} = 311$ K [13], with a low temperature magnetic moment amplitude of $0.62\mu_\mathrm{B}$. The SDW is well understood from band structure calculations [14–16] and arises from the nesting of $3d$ electron and hole Fermi surfaces by a propagation vector $q = (2\pi/a)(1 \pm \delta)$ [17]. Magnetic moments are arranged perpendicular to the propagation vector ($\boldsymbol{\mu} \perp \mathbf{q}$)

---

[a] Also, Max-Planck-Institute für Metallforchung, Heisenbergstr. 1, 70569, Stuttgart, Germany
e-mail: `danny@esrf.fr`

in the temperature range 122 K $\leq T \leq T_{\mathrm{N}}$ [18] in a so-called transverse spin density wave (TSDW). However, several structures are compatible with the magnetic diffraction pattern. Originally, an antiphase domain ordering was proposed [19,20], but subsequent investigations of the third order harmonic satellites [21] were found to be incompatible with this structure. Helical [22,23] and sinusoidal linear [24] spin density wave configurations, have also been supposed. A spin reorientation occurs below $T_{\mathrm{SF}} = 122$ K [25]; the magnetic moments flip parallel to the propagation vector ($\boldsymbol{\mu} \parallel \mathbf{q}$) and a longitudinal spin density wave (LSDW) is formed. In this phase, the spin density wave can only be linear, so that the spin flip transition is fairly convincing evidence against the formation of a helical SDW in the high temperature phase. Polarised neutron scattering studies [26] also corroborate this assumption. Nevertheless, there is some controversy over the direct observation of a *linear* SDW and associated polarisation domains (S_x and S_y) [27–29], above T_{SF} [30]. In our investigations, the NRXMS azimuthal dependence gives decisive evidence confirming the formation of a *linear* SDW together with two polarisation domains in the TSDW phase. These measurements are discussed in Section 3.

Magnetic-field dependence neutron measurements [31,32] have demonstrated that chromium comprises a single-Q structure. Three Q domains (Q_x, Q_y and Q_z) are formed in different regions of the crystal, each containing a single magnetisation wave. These domains give rise to six magnetic satellites in reciprocal space. Upon field-cooing, chromium crystals form a single-Q domain, for which there are only two magnetic satellites in reciprocal space. The dimensions of the Q domains have been estimated from topography measurements to be relatively large $\sim 1-2$ mm^3 [27–29]. The chromium spin and charge density waves have been the subject of previous X-ray diffraction publications [33,34]. These investigations report the observation of single-Q phase chromium despite the fact that neither sample had been field cooled. The domain structure of chromium is addressed in Sections 2 and 3.

RXMS is an element specific spectroscopy occurring when the incident photon energy matches roughly that of an absorption edge [5,6]. The enhancement of the magnetic intensity was first explained by Hannon [6], as arising from electric dipole ($E1$) or quadrupole ($E2$) transitions to available states above the Fermi level. Excitations at K absorption edges, involve transitions from core $1s$ to the $4p$ ($E1$) and $3d$ ($E2$) states. The core $1s$ level is not spin orbit split and these resonances generally rely on spin orbit effects in the intermediate states. Consequently, the magnetic enhancement is expected to be weaker than at the spin orbit split $\mathrm{L}_{2,3}$ and M_{2-5} edges. At these spin-orbit split edges, sum rules [35] on the imaginary part of the magnetic scattering amplitude can be used to determine $\langle \mathbf{L} \rangle$. At K edges it appears that the quadrupole resonance is proportional to $\langle \mathbf{L} \rangle$ [36]; such a conclusion can also be drawn from Hannon's model [37]. Therefore, in the absence of orbital polarisation in an atomic ground state (such as that demonstrated unambiguously for chromium in Sect. 3), no quadrupole resonance is predicted. RXMS with polarization analysis has not been previously reported from chromium. We have taken advantage of a high flux undulator beamline at a third generation synchrotron, using polarisation analysis, for a renewed understanding of the resonant processes in this material. These investigations are described in Section 4.

2 Experimental

The chromium sample was grown by iodide vapour transport [38,39] and has approximate dimensions $\sim 5 \times 5 \times 5$ mm^3. The examined surface was grown with a (001) face and was not treated by mechanical polishing or chemical etching. The sample was found to be highly pure spectrally and this is also supported by the observed value of the Néel temperature. The crystal was mounted on the cold finger of a closed cycle refrigerator and sealed in a beryllium cap with helium exchange gas. Using 16 keV photons, the crystal mosaic the (004) reflection was found to be 0.008°, indicating that the crystal was excellent quality.

Our experiments were undertaken at the ID20 magnetic scattering undulator beamline [40] of the European Synchrotron Radiation Facility. Two, phased, 42 mm period undulators deliver linear σ-polarised photons perpendicular to the diffraction (in this case vertical) plane. The incident beam energy is selected by a silicon (111) double crystal monochromator; the second crystal bends to provide sagittal beam focus. Two curved Si-Rh dual-track mirrors, astride of the monochromator, suppress higher order contamination and focus the beam in the vertical direction. The primary slits, prior to the optical elements, were closed around the central cone of the first harmonic of the undulators to 1.2×0.8 mm^2. At 5.219 keV the photon flux measured at the sample position was 7×10^{12} photons/s/200 mA, with 99.8% polarisation in a focussed spot-size of 0.2×0.3 mm^2.

In addition to the standard four circle axes (θ, 2θ, χ, and ϕ) of the diffractometer, a specially designed azimuthal circle was mounted on the ϕ rotation. This axis has been specifically incorporated for Renninger type scans [41] about the surface normal, nominally designated azimuthal Φ (see Fig. 1). In specular geometry, this involves rotations about the scattering vector $\mathbf{Q}$. In X-ray magnetic scattering experiments, a standard co-ordinate system [3] can be constructed around the centre of rotation of the diffractometer. This system comprises the components of the sample magnetisation in terms of the incident and exit wave vectors k_i and k_f along three orthogonal axes U_1, U_2 and U_3 (see Fig. 1). U_1 is directed along the incident and scattered wave vectors $k_{\mathrm{i}} + k_f$, U_2 along the cross product of k_i and k_f, perpendicular to the scattering plane and U_3 is directed antiparallel to $\mathbf{Q}$. The cross-section for σ and π incident polarisations are expressed for the magnetisation components along these directions. The sample was aligned with a four-fold axis in the diffraction plane (parallel to U_1 in Fig. 1), nominally designated azimuthal $\Phi =$ zero (see Fig. 3). At this

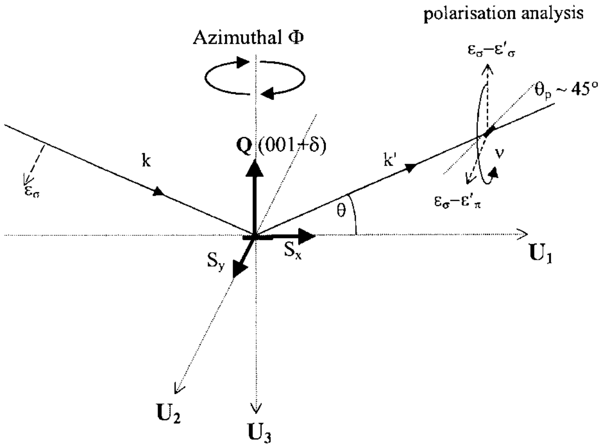

Fig. 1. Incident σ-polarised photons with wave vector k, are diffracted from the sample with scattered wave vector k'. The specular (001+δ) spin density wave was studied in both non-resonant and resonant scattering regimes. The sample is aligned with the crystal four-fold axis along parallel to the scattering plane which is defined as azimuthal $\Phi = 0$. At this value of Φ, the S_x polarisation domain has magnetic moments parallel to U_1 and the S_y domain has magnetic moments directed along U_2. The standard axes U_i (i = 1, 2, 3) is discussed in the text. The magnetic scattering from the two polarisation domains is averaged by azimuthal Φ.

value of Φ, the two polarisation domains formed in a linear TSDW phase are defined in Figure 1. The S_x domain, comprises a SDW, with magnetic moments directed along U_1 and the S_y domain, contains a SDW, with magnetic moments directed along U_2. For a helical SDW, the moments would spiral in the plane perpendicular to **Q**. These polarisation domains could be unequally populated within the scattering volume of the crystal. This is especially true for chromium, which has relatively large domain dimensions. Therefore, the azimuthal dependence is required to average the scattering from the domains, for an accurate determination the L/S ratio.

Polarisation analysis of the scattered intensity was used in both the non-resonant and resonant scattering regimes (see Fig. 1). Appropriate analyser crystal reflections are selected to give Bragg angles (θ_p) close to 45°. For the non-resonant scattering studies, 5.219 keV photons in combination with a graphite (004) analyser (of 8% measured peak reflectivity) were used. This energy is selected below the chromium K-absorption edge to reduce the background from fluorescence and to give an analyser Bragg angle (θ_p) of exactly 45°. These photons probe the sample to a depth of $\approx$ 17 μm. In the resonant scattering regime, the incident X-ray energy was tuned to the chromium K-absorption edge $\sim$ 5.989 keV. An Al (220) analyser crystal (of 4% measured peak reflectivity) was used for polarisation analysis. At this energy, the analyser Bragg angle (θ_p) is $\approx 47.2°$ and the photons probe a region of the surface to approximately 3 μm.

The (001+δ) SDW intensity at 5.219 keV was $\sim$ 6000 cts/sec at 200 mA synchrotron current, without polarisation analysis. The pre-sample slits where set to 0.4×0.4 mm^2 so that illuminated footprint on the sample at the (001+δ) SDW (Bragg angle of 25.59° at 5.219 keV) was $\sim 0.4 \times 1.0$ mm^2. Only (001$\pm\delta$) like magnetic reflections were observed and no evidence for off-specular satellites could be found, indicating that the sample region within the illuminated footprint was entirely single-Q. It has been suggested that a single domain state could arise from surface strain effects [33]. However, we have additionally observed this single domain state using 25 keV photons to probe the bulk of the sample (60 mm). The observation of a single-Q state in this experiment is consistent with the fact that the beam does not probe the entire sample. X-ray topography experiments on our chromium sample [42] also indicate large > 2 mm^3 domain sizes.

3 Non-resonant X-ray magnetic scattering

The components of the orbital (L) and spin (S) magnetic moments in the NRXMS regime are defined within the standard co-ordinate system in Figure 1 as L_i and S_i (i = 1, 2, 3). For incident σ polarised photons, the NRXMS scattering amplitude is [1],

$$f_{\text{non-res}} = \begin{bmatrix} f_{\sigma\to\sigma} \\ f_{\sigma\to\pi} \end{bmatrix} = -\mathrm{i}\frac{\hbar\omega}{mc^2} r_0 \times \begin{bmatrix} \sin 2\theta S_2(Q) \\ 2\sin^2\theta\cos\theta\,[L_1(Q) + S_1(Q)] + \left(\sin^2\theta S_3(Q)\right) \end{bmatrix}, \tag{3.1}$$

where, $\hbar\omega$ is the incident energy and r_0 is the classical electron radius. The different polarisation dependence of L and S components, leads to the possibility of spin and orbit moment separation using polarisation analysis [43,44]. The magnetisation components L_i and S_i, in equation (3.1), can be expressed in terms of the azimuthal-Φ rotation angle, as,

$$\begin{aligned} S_1(Q) &= S(Q)\sin\Phi, \\ L_1(Q) &= L(Q)\sin\Phi, \\ S_2(Q) &= S(Q)\cos\Phi. \end{aligned} \tag{3.2}$$

Here we have assumed that **L** and **S** are colinear and the formation of a linear SDW. The L/S ratio, for the azimuthal averaged intensities, follows from equation (3.1) as

$$\frac{L(Q)}{S(Q)} = \frac{1}{\sin\theta}\sqrt{\frac{I_\Phi^{\sigma\pi}}{I_\Phi^{\sigma\sigma}} - 1}\cdot \tag{3.3}$$

$I_\Phi^{\sigma\sigma}$ and $I_\Phi^{\sigma\pi}$ are the Φ averaged intensities, corrected by the different analyser rocking curve widths for the $\sigma\sigma$ and $\delta\pi$ polarisations. An azimuthal dependence is not expected for a helical SDW because the moments are isotropic in the basal plane for this structure. Therefore, in the TSDW phase, the azimuthal intensities give unique insight into the nature of the chromium spin density wave,

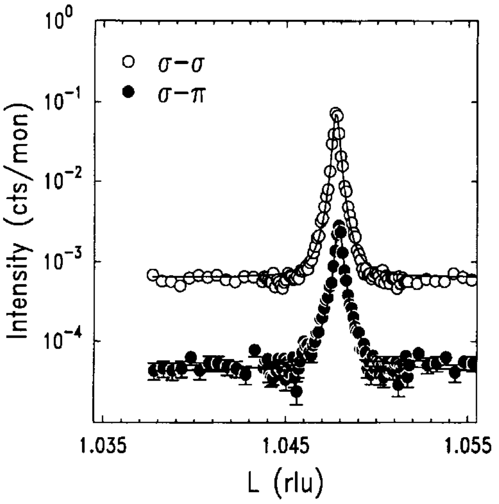

Fig. 2. Typical radial scans normal to the surface (parallel to Q) in the non-resonant regime used to integrate the scattered intensities in the $\sigma\sigma$ (open circles) and $\sigma\pi$ (solid circles) channels. The data are on a logarithmic scale and the larger background for the $\sigma\sigma$ polarisation is from the specular charge rod. The solid lines are Lorentzian fits to the data.

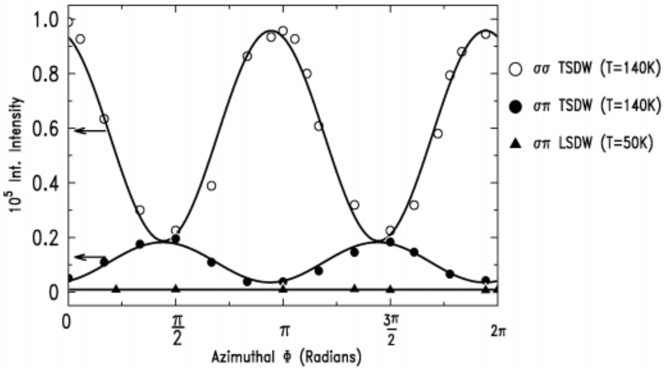

Fig. 3. The azimuthal dependence of the $\sigma\sigma$ (open circles) and $\sigma\pi$ (solid circles) non-resonant scattering in the transverse spin density wave phase ($T = 140$ K). The solid line is a fit, giving $L/S = 0$. The data give unique evidence that chromium forms a linear polarised spin density wave. The solid triangles are data taken in the LSDW phase ($T = 50$ K). No azimuthal dependence is expected in this phase.

directly confirming if it is linear from an observed periodicity. In the LSDW phase, the polarisation flips parallel to $\mathbf{Q}$ and no magnetisation components are rotated in Φ around the scattering vector. Consequently, no azimuthal dependence is expected in this phase.

Only $(001\pm\delta)$ SDW magnetic reflections are accessible at 5.219 keV, due to the relatively small lattice parameter ($a_0 = 2.88$ Å). Radial scans normal to the surface (parallel to $\mathbf{Q}$) of the $(001+\delta)$ spin density wave reflection, are compared in Figure 2. The magnetic peaks are resolution limited, so that it is not possible to extract an exact correlation length for the S domain from the widths. However, a lower limit of ~ 4000 Å can be deduced. A larger background for the $\sigma\sigma$ polarisation arises from the specular ridge and this is accounted for in the Lorentzian fits to the data. The $\sigma\sigma$ and $\sigma\pi$ scattered polarisations were collected for several azimuthal angles (Φ) and their integrated intensities are shown in Figure 3. The open circles are for the $\sigma\sigma$ intensities and the solid circles for the $\sigma\pi$, in the TSDW phase ($T = 140$ K). This figure demonstrates that chromium indeed forms a *linear* spin density wave because of the observed azimuthal periodicity. The intensities exhibit a two-fold symmetry, consistent with an almost entirely single polarisation domain population. Since the intensities do not go to zero at $\Phi = 90°$, the scattering volume cannot be completely single domain (Eq. (3.2)). Domain volume fractions, $v_y = 0.83 \pm 0.03$ and $v_x = 0.17 \pm 0.03$, of the S_y and S_x polarisation domains, have been deduced from Figure 3. The size of the S domains could have been further investigated by translating the sample in the X-ray beam. However, this kind of analysis was not undertaken. The solid line is a fit using equation (3.2) and gives the $\sigma\sigma$ and $\sigma\pi$ intensities averaged across the v_x and v_y domain volumes. These values are marked with an arrow on the left hand axis and correspond to $I_\Phi^{\sigma\sigma} = (5.7 \pm 0.1) \times 10^{-6}$ and $I_\Phi^{\sigma\pi} = (1.08 \pm 0.06) \times 10^{-6}$. From equation (3.3), this gives a ratio of $L/S = 0.008 \pm 0.03$. The orbital magnetisation in chromium is therefore zero (less than 1%). To the accuracy of these measurements, an upper limit of 3% orbital density can be deduced. This negligible value of $\langle L \rangle$ is expected for $3d^5$ electronic ground state of chromium. The solid triangles in Figure 3 are the $\sigma\pi$ intensities in the LSDW phase ($T = 50$ K), the weaker intensity arises from the geometrical terms for S_3 in equation (3.1). No azimuthal dependence is observed in this phase as anticipated for $\mathbf{S} \parallel \mathbf{Q}$. The $\sigma\sigma$ intensities are zero below T_{SF}, because the magnetisation components along S_3 rotate the incident polarisation.

From this direct measurement of zero orbital magnetisation in chromium, we discuss in Section 4 the RXMS by considering both the non-resonant and resonant amplitudes. For this purpose, it is convenient to write the spin only ($L = 0$) non-resonant amplitude from equation (3.1) as,

$$f_{\mathrm{nonres}}(\mathbf{Q}) = \begin{bmatrix} f_{\mathrm{nonres}}^{\sigma\sigma} \\ f_{\mathrm{nonres}}^{\sigma\pi} \end{bmatrix} = -\mathrm{i}\frac{\hbar\omega}{mc^2} r_0 2S f_{\mathrm{m}}(Q) \sin\theta \times \begin{bmatrix} \mathbf{z}_2 \cos\theta \\ \sin\theta\,[\mathbf{z}_1 \cos\theta + \mathbf{z}_3 \sin\theta] \end{bmatrix}. \quad (3.4)$$

Here, $2S$ is the ordered magnetic moment, $f_{\mathrm{m}}(Q)$ is the spin only form factor and $\mathbf{z}_{1,2,3}$ are unit vectors along the magnetisation direction $U_{1,2,3}$ shown in Figure 1. A prefactor of $|f_{\mathrm{nonres}}| = 2S(\hbar\omega/mc^2)r_0 \approx 5 \times 10^{-3} r_0$ can be determined to the geometrical terms in equation (3.4). This value is then used in the models of the resonant scattering described in the next section.

4 Resonant X-ray magnetic scattering

The RXMS dipole and quadrupole amplitudes are conveniently given by Hill and McMorrow [45]. For incident σ-polarised photons the dipole resonant magnetic scattering amplitude is,

$$f_{E1}^{\mathrm{res1}} = \begin{bmatrix} f_{E1}^{\sigma\sigma} \\ f_{E1}^{\sigma\pi} \end{bmatrix} = \frac{A_{E1}}{[(E_{\mathrm{a}} - E_{\mathrm{c}} - \hbar\omega_{E1})/(\Gamma/2) - \mathrm{i}]} \times \begin{bmatrix} 0 \\ \mathbf{z}_3 \sin\theta - \mathbf{z}_1 \cos\theta \end{bmatrix}. \quad (4.1)$$

A_{E1} determines the strength of the magnetic scattering (at the magnetic wave-vector) and is related to atomic overlap integrals between initial and excited states. The denominator describes the deviation from resonance in units of the core hole lifetime Γ and accounts for the Lorentzian profile of the resonance. E_{a} is the energy of the initial state and E_{c} is the energy of the excited intermediate state. Typical values of A_{E1} for transition metals are $\approx 10^{-2} r_0$ [37,46]. A similar expression can be written for quadrupole transitions, considered later. The total magnetic scattering amplitude is the sum of the non-resonant (Eq. (3.4)) and resonant (Eq. (4.1)) contributions.

The absorption coefficients in the vicinity of the chromium K absorption edge, extracted from fluorescence spectra [47], are shown in Figure 4a. The solid line is a fit to the data, consisting of an arctangent function to describe the absorption step function and a Lorentzian function in the white line region. Additional peaks are later added to account for the EXAFS oscillations after the edge. By careful fitting of the pre-edge tail a value of the core-hole life time of $\Gamma = 1.1 \pm 0.5$ eV was obtained [48]. The measured RXMS peaks are slightly broader than this due to finite energy resolution effects.

The integrated intensities of the $(001{+}\delta)$ spin density wave, in the vicinity of the chromium K edge ($E = 5.989$ keV), taken at an azimuthal angle $\Phi = 0$, are shown in Figures 4b–d. The open circles in Figure 4b are for the $\sigma\sigma$ scattered polarisation in the TSDW ($T = 140$ K) phase and the corresponding $\sigma\pi$ polarisation are the solid circles in Figure 4c. Solid triangles in Figure 4d represent the $\sigma\pi$ intensities in the LSDW phase ($T = 50$ K). These data have not been corrected for absorption, but corrections have been made for cross-talk [49], due to the deviation from 45° of the analyser crystal Bragg angle. RXMS is observed, as shown in Figures 4c and d. The peak appears only for the $\sigma\pi$ scattered polarisation and occurs in the white line energy region. These are strong indications that the resonance arises from dipole transitions to the $4p$ states. Quadrupole resonant magnetic scattering, expected in both $\sigma\sigma$ and $\sigma\pi$ polarisations, below the K edge, is not observed. The absence of the quadrupole resonance is in good qualitative agreement with theory for zero orbital moment.

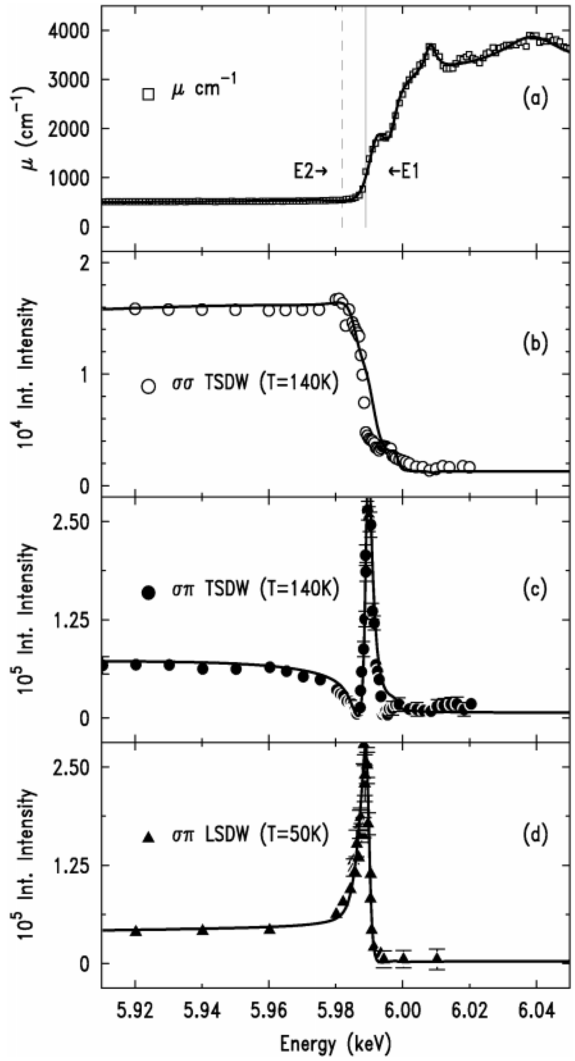

Fig. 4. (a) Absorption coefficients obtained from the fluorescence taken in the vicinity of the K absorption edge. (b) The $\sigma\sigma$ resonant magnetic scattering in the TSDW phase. (c) The $\sigma\pi$ resonant scattering intensity in the TSDW phase. (d) The $\sigma\pi$ resonant scattering in LSDW phase. The solid lines are fits using the models described in the text.

To model the energy profiles in Figures 4b–d, we have initially considered a single dipole resonant magnetic amplitude, together with interference from the non-resonant magnetic amplitude. The total magnetic scattering intensities for the $\sigma\sigma$ and $\sigma\pi$ polarisations in the different temperature phases of chromium are,

$$I_{\mathrm{TSDW}}^{\sigma\sigma}(\Phi) = A_{\mathrm{SF}} \sum_{i=x,y} \nu_i |f_{\mathrm{nonres}}^{\sigma\sigma}(\Phi, i)|^2 \quad (4.2)$$

$$I_{\mathrm{TSDW}}^{\sigma\pi}(\Phi) = A_{\mathrm{SF}} \sum_{i=x,y} \nu_i \times \left| \left[f_{\mathrm{nonres}}^{\sigma\pi}(\Phi, i) + \frac{A_{E1}[-\mathbf{z}_1(\Phi, i)\cos\theta]}{[(E_{\mathrm{a}} - E_{\mathrm{c}} - \hbar\omega_{E1})/(\Gamma/2) - \mathrm{i}]} \right] \right|^2 \quad (4.3)$$

$$I_{\mathrm{LSDW}}^{\sigma\sigma} = 0 \quad (4.4)$$

$$I_{\mathrm{LSDW}}^{\sigma\pi} = A_{\mathrm{SF}} \left| \left[f_{\mathrm{nonres}}^{\sigma\pi} + \frac{A_{E1}[\mathbf{z}_3 \sin\theta]}{[(E_{\mathrm{a}} - E_{\mathrm{c}} - \hbar\omega_{E1})/(\Gamma/2) - \mathrm{i}]} \right] \right|. \quad (4.5)$$

Since the measured intensities are not on an absolute scale, the scale factor A_{SF} is used. The $v_i (i = x, y)$ refer to the volume fractions of the x and y domains, present in the TSDW phase. The scattered intensity from these domain volumes depends on the azimuthal angle Φ (Eqs. (4.2, 4.3)). At $\Phi = 0$, the scattering from the two domains may be separated with polarisation analysis, provided that $\mathbf{L} = 0$. In the LSDW phase, there can only be one domain volume, since $\mathbf{S} \parallel \mathbf{Q}$. The scattered intensity does not depend on the azimuthal angle below T_{SF} (Eq. (4.5)) and the incident σ-polarised photons are scattered with a change of polarisation (Eq. (4.4)). The solid lines in Figures 4b–d are fits using equations (4.2–4.5). The chromium crystal had an extended face and the change in absorption across the K edge region was accounted for by dividing the calculated integrated intensities by the absorption coefficients (Fig. 4a). In our models, we have assumed that the domain fractions do not change as a function of photon penetration depth.

The relative domain volumes deduced from the azimuthal dependence in section 3 $v_y = 0.87$ and $v_x = 0.13$ were used in the fits to data in the TSDW phase (Figs. 4b, c). In order to model these data, f_{nonres} was kept constant at its calculated value of $5.0 \times 10^{-3} r_0$, with the geometrical factors in equation (3.4). For the $\sigma\sigma$ intensities, in Figure 4b, the scale factor is the only variable. The solid line fit is in very good agreement with the data and shows that the energy profile arises from the change in absorption for this polarisation. Note, that this figure is equivalent to Figure 5 in reference [33], measured without polarisation analysis and for which resonant magnetic scattering is not observed. The obtained value of $A_{\mathrm{SF}} = 1.0 \pm 0.2$, was subsequently used to model the TSDW $\sigma\pi$ data in Figure 4c. In this fit to the data, the variables were A_{E1}, $\hbar\omega_{E1}$ and Γ, which were found to be $A_{E1} = 3.2 \pm 0.2 \times 10^{-3} r_0$, $\hbar\omega_{E1} = 5.989 \pm 0.001$ keV and $\Gamma = 2.4 \pm 0.5$ eV. The observed Γ is significantly broader than that deduced from the fluorescence (1.1 eV). This broadening reflects the band character of the p states in chromium. The values of A_{E1}, $\hbar\omega_{E1}$ and Γ obtained, were then used in the fit to the $\sigma\pi$ LSDW data, in Figure 4d. The domain volume fraction was assumed to be one and only variable was the scale factor, which was found to be $A_{\mathrm{SF}} = 0.9 \pm 0.2$. This value is in very good agreement with the one deduced in the TSDW phase, in good accord with the expectation of a single polarisation state in this phase. This value also suggests that chromium remains single-Q across this temperature range. The apparent shift in position and shape if the $\sigma\pi$ intensities of Figures 4c and 4d, arises from a change of sign in the interference between non-resonant and resonant scattering amplitudes. This is described by the $\mathbf{z}_1$ and $\mathbf{z}_3$ components in the dipole cross-section (Eq. (4.1)). The fits to the energy profiles are slightly improved by allowing for a small quadrupole amplitude of $3 \times 10^{-4} r_0$ at an energy $\hbar\omega_{E2} = 5.985$ keV. This gives an upper limit to the quadrupole amplitude of at least one order of magnitude smaller than that of the dipole. Similar weak quadrupole amplitudes have been determined for other $3d^5$ compounds, $\mathrm{RbMnF_3}$ [46] and MnO [50]. The values for the dipole and quadrupole amplitudes, found from our models of the RXMS in chromium, are consistent with those derived in [41,45], taking into account the smaller magnetic moment of chromium. The agreement together with the good fit to the data in Figure 4, gives confidence in the validity of this approach and to the quadrupole model developed in [37].

5 Conclusions

Our investigations using X-ray magnetic scattering with polarisation analysis, give a fresh and unequivocal insight into the fascinating magnetic properties chromium. The small X-ray beam size individually probes the relatively large Q domains and our NRXMS investigations give direct evidence for the formation of two polarisation S domains in the TSDW phase. The models used in the resonant scattering regime also support the formation of two polarisation domains in the TSDW phase and a single domain in the LSDW phase. The NRXMS azimuthal dependence provides unique evidence that chromium forms a linear polarised spin density wave. We have subsequently used these intensities, to determine directly zero orbital magnetic moment in chromium. This value of $\mathbf{L} = 0$, is expected for the chromium electronic configuration. We have reported on resonant X-ray magnetic scattering from chromium, using polarisation analysis, for the first time. A consistent model of the energy profiles has been derived in this energy regime, from the resonant and non-resonant scattering amplitudes. The scattering arises primarily from dipole transitions to the $4p$ states. Since the $3d$ states are of most interest to the understanding the magnetism of chromium, it is natural the band structure calculations have focussed mainly on the $3d$ band and little work has been published on the $4p$ spin polarisation. However, further calculations of the $4p$ density of states are needed to provide a more quantitative model of the dipole RXMS described in this paper. RXMS involving quadrupole transitions to the $3d$ band, was not observed. This effect can be understood from recent models of the role of the orbital moment in $3d$ K-edge quadrupole resonances. For the specific case of the $3d^5$ ion, the scattering amplitude is zero. The derived resonant and non-resonant amplitudes from our model are completely consistent with values for other $3d^5$ systems, for example $\mathrm{RbMnF_3}$ and MnO. Dipole transitions, probing the chromium $3d$ states, are allowed at the spin orbit split L absorption edges of chromium. These edges are generally too low in energy (~ 600 eV) for scattering experiments, but would offer an interesting challenge to studies of long periodic materials such as multilayers.

DM thanks W. Neubeck and R. Chagnon for their dedication in the development of the azimuthal apparatus at ID20. Fruitful discussions were held with W. Neubeck on the subject of $3d$ transition metal resonances and their spin and orbital magnetic moments. DM acknowledges the European Commission for support given in the frame of the program

"Training and Mobility of Researchers". P.C.d.C, thanks Conselho Nacional de Desenvolvimento Científico e Tecnológico (CNPq) and A.J.A.d.O acknowledges de PADCT- III (CNPq) and Fundação de Amparo à Pesquisa do Estado de São Paulo (FAPESP) for financial support. C.G. acknowledges financial support from FAPESP under contract 96/05586-6 and CNPq.

References

1. F. de Bergevin, M. Brunel, Acta Cryst. A **37**, 314 (1981).
2. M. Blume, J. Appl. Phys. **57**, 3615 (1985).
3. M. Blume, D. Gibbs, Phys. Rev. B. **37**, 1779 (1988).
4. K. Namikawa, T. Nakajima, K. Kowata, J. Phys. Soc. Jpn **54**, 4099, (1985).
5. D. Gibbs, D.R. Harshmann, E.D. Isaacs, D.B. McWhan, D. Mills, C. Vettier, Phys. Rev. Lett. **61**, 1241 (1988).
6. J.P. Hannon, G.T. Trammell, M. Blume, D. Gibbs, Phys. Rev. Lett. **61**, 1245 (1988).
7. A.J. Freeman, R.E. Watson. Acta. Cryst. **14**, 231 (1961).
8. R.M. Moon, W.C. Koehler, A.L. Trego, J. Appl. Phys. **37**, 1036 (1966).
9. C. Stassis, G.R. Klein, S.K. Sinha, Phys. Rev. Lett. **31**, 1498 (1973).
10. Strempfer, T. Brückel, W. Caliebe, G. McIntyre, F. Tasset, T. Zeiske, K. Burger, W. Prandl, J.R. Schneider, Eur. Phys. J. B **14**, 63 (2000).
11. H.A. Alperin, J. Phys. Soc. Jpn **17**, 12 (1962); Phys. Rev. Lett. **6**, 55 (1961).
12. V. Fernandez, C. Vettier, F. de Bergevin, C. Giles, W. Neubeck. Phys. Rev. B. **57**, 7870 (1998).
13. E. Fawcett, Rev. Mod. Phys. **60**, 209 (1988).
14. J. Kübler, J. Magn. Magn. Mater. **20**, 277 (1980).
15. P.E.S Persson, L.I. Johansson, Phys. Rev. B **33**, 8814 (1986).
16. V.L. Moruzzi, A.R. Williams, J.F. Janak, *Calculations in electronic properties of metals* (Pergamon, New York, 1978).
17. A.W. Overhauser, Phys. Rev. Lett. **3**, 414 (1959).
18. C.G. Shull, M. K. Wilkinson, Rev. Mod. Phys. **25**, 100 (1953).
19. L.M. Corliss, J.M. Hastings, Phys. Rev. Lett. **3**, 211 (1959).
20. G. E. Bacon, Acta Cryst. **14**, 823 (1961).
21. G. Shirane, W.J. Takei, Phys. Soc. Jpn **17**, Suppl. B-111, 35 (1962).
22. T.A. Kaplan, Phys. Rev. **116**, 888 (1959).
23. B.R. Cooper, Phys. Rev. **118**, 135 (1960).
24. A.W. Overhauser, A. Arrott, Phys. Rev. Lett. **4**, 226 (1960).
25. J. Hastings, Bull. Am. Phys. Soc. **5**, 455 (1960).
26. P.J. Brown, C. Wilkinson, J.B. Forsyth, R. Nathans, Proc. Phys. Soc. **85**, 1185 (1965).
27. M. Ando, S. Hosoya, Phys. Rev. Lett. **29**, 281 (1972).
28. M. Ando, S. Hosoya, J. Appl. Phys. **49**, 6045 (1978).
29. S. Hosoya, M. Ando, Phys. Rev. Lett. **26**, 321 (1971).
30. See for example the discussion on polarisation S domains in reference [7] Section IV.C p. 275 and the references therein.
31. S.A. Werner, A. Arrnott, H. Kendrick, J. Appl. Phys. **37**, 1260 (1966).
32. R. Street, B.C. Munday, B. Windows, J. Appl. Phys. **39**, 1050 (1968).
33. J.P. Hill, G. Helgesen, D. Gibbs, Phys. Rev. B. **51**, 10336 (1995).
34. D. Gibbs, K.M. Mohanty, J. Boar, Phys. Rev. B. **37**, 562 (1988).
35. P. Carra, M. Altarelli, Phys. Rev. Lett. **64**, 1286 (1990).
36. S.W. Lovesey, J. Phys. Cond. Matt. **10**, 2505 (1998).
37. W. Neubeck, C. Vettier, F. de Bergevin, F. Yakhou, D. Mannix, O. Bengone, M. Alouani, A. Barbier (to be published).
38. H. Winterha, U. Holtkamp, Metal **22**, 33 (1968).
39. *Chemical Transport Reactions*, H. Schäfer (Academic Press, 1964).
40. A. Stunault, C. Vettier, F. de Bergevin, N. Bernhoeft, V. Fernandez, S. Langridge, E. Liström, J.E. Lorenzo-Diaz, D. Wermeille, L. Chabert, R. Chagnon. Synch. Rad. **5**, 1010 (1998).
41. M. Renninger, Z. Phys. **106**, 141–176, (1937).
42. P.C. de Camargo, A.J.A. de Oliveria, J. Baruchel (unpublished).
43. D. Gibbs, G. Grübel, D.R. Harshmann, E.D. Isaacs, D.B. Mcwhan, D. Mills, C. Vettier. Phys. Rev. B. **43**, 5663 (1991).
44. S. Langridge, G.H. Lander, N. Bernhoeft, A. Stunault, C. Vettier, G. Grübel, S. Sutter, F. de Bergevin, W.J. Nuttall, W.G. Stirling, K. Mattenburger, O. Vogt. Phys. Rev. B. **55**, 6392 (1997).
45. J.P. Hill, D.F. McMorrow. Acta. Crystallogr. A **52**, 236 (1996).
46. A. Stunault, F. de Bergevin, D. Wermeille, C. Vettier, T. Brükel, N. Bernhoeft, G.S. McIntyre, J.Y. Henry, Phys. Rev. B **60**, 10170 (1999).
47. S. Eisebitt, T. Boske, J.E. Rubensson, E. Eberhardt. Phys. Rev. B. **47**, 14103 (1993).
48. F. de Bergevin, M. Brunel, R.M. Galera, C. Vettier, E. Elkaim, M. Bessiere, S. Lefebvre, Phys. Rev. B **37**, 1779 (1998).
49. F. Vaillant, Acta Crystallogr. A **33**, 967 (1977).
50. W. Neubeck Ph.D. thesis, Université Joseph Fourier, Grenoble, 2000.